Towards the parallelization of Reversible Jump Markov Chain Monte Carlo algorithms for vision problems.

Yannick Verdié , Florent Lafarge

RESEARCH REPORT
N° 8016
July 2012
Project-Teams Geometrica, Ayin

ISSN 0249-6399 ISRN INRIA/RR--8016--FR+ENG

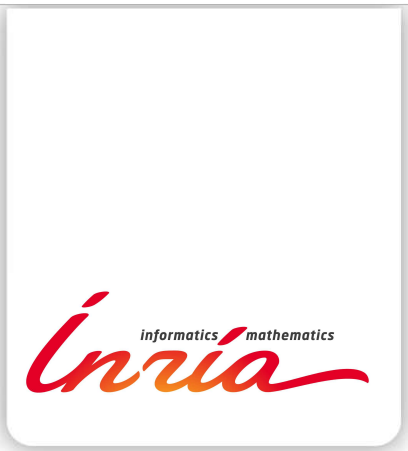

Towards the parallelization of Reversible Jump Markov Chain Monte Carlo algorithms for vision problems.

Yannick Verdié *, Florent Lafarge *

Project-Teams Geometrica, Ayin

Research Report n° 8016 — July 2012 — 33 pages

Abstract: Point processes have demonstrated efficiency and competitiveness when addressing object recognition problems in vision. However, simulating these mathematical models is a difficult task, especially on large scenes. Existing samplers suffer from average performances in terms of computation time and stability. We propose a new sampling procedure based on a Monte Carlo formalism. Our algorithm exploits Markovian properties of point processes to perform the sampling in parallel. This procedure is embedded into a data-driven mechanism such that the points are non-uniformly distributed in the scene. The performances of the sampler are analyzed through a set of experiments on various object recognition problems from large scenes, and through comparisons to the existing algorithms.

Key-words: Image and vision, Stochastic Model, Monte Carlo, energy minimization, Markov Random Field

* INRIA Sophia Antipolis, France

RESEARCH CENTRE
SOPHIA ANTIPOLIS – MÉDITERRANÉE

2004 route des Lucioles - BP 93
06902 Sophia Antipolis Cedex

Vers la parallélisation des algorithmes de Monte Carlo par chaine de Markov à sauts réversibles pour les problèmes en vision.

Résumé : Les processus de ponctuels marqués se sont montrés extrêmement performants pour traiter des problèmes de detection d'objects et reconnaissance de formes en vision par ordinateur. Cependant, la simulation de ces modèles mathématiques est une tache difficile, en particulier pour des scènes larges. Les échantillonneurs existant souffrent de performances moyenne en terme de temps de calcul et de stabilité. Nous proposons un nouvel algorithme exploitant les propriétés markoviennes des processus de points afin d'effectuer un échantillonnage en parallèle. Cette méthode est intégrée à un mechanisme guidé par les données afin d'obtenir une distibution non uniforme des points dans la scène. Les performances de ce nouvel échantillonneur sont analysées à travers plusieurs expériences sur de larges scènes et comparées aux algorithmes existants.

Mots-clés : Image et vision, modèle stochastique, Monte Carlo, minimisation d'energie, champ de Markov

1 Introduction

Markov point processes constitute an object-oriented extension of traditional Markov Random Fields (MRF). Whereas MRFs address labeling problems on static graphs, Markov point processes can tackle object recognition problems by directly manipulating parametric entities on dynamic graphs. These probabilistic models introduced by Baddeley *et al.* [1] exploit random variables whose realizations are configurations of parametric objects, each object being assigned to a point positioned in the scene. The number of objects is itself a random variable, and thus must not be estimated or specified by an user. Another strength of Markov point processes is their ability to take into account complex spatial interactions between the objects and to impose global regularization constraints.

1.1 Point processes for vision problems

Many recent works exploiting point processes have been proposed to address a large variety of computer vision problems [2, 3, 4, 5, 6, 7, 8, 9]. The growing interest in these probabilistic models is motivated by the need to manipulate parametric objects interacting in scenes. Parametric objects can be defined in discrete and/or continuous domains. They usually correspond to geometric entities, *e.g.* segments, rectangles, circles or planes, but can more generally be any type of multi-dimensional function. A point process requires the formulation of a probability density in order to measure the quality of a configuration of objects. The density is typically defined as a combination of a term assessing the consistency of objects to the data, and a term taking into account spatial interactions between objects in a Markovian context. The optimal configuration maximizing this density is usually searched for by a Monte Carlo based sampler capable of exploring the whole configuration space, in most cases a Markov Chain Monte Carlo (MCMC) algorithm [10, 11].

Descombes *et al.* [2] propose a point process for counting populations from aerial images, each entity being captured by an ellipse. Ge *et al.* [3] present a point process for a similar application, but dedicated to crowd detection from ground-based photos, for which objects are defined as a set of body shape templates learned from training data. Multi-view images are used by Utasi *et al.* [9] to detect people by a point process in 3D where the objects are specified by cylinders. Sun *et al.* [8] and Lacoste *et al.* [7] propose point processes for extracting line networks from images by taking into account spatial interactions between lines to favor the object connexion. Lafarge *et al.* [4] present a general model for extracting different types of geometric features from images, including line, rectangles or disks. A mixture of object interactions are also considered such that the process can address different problems ranging from population counting to line network extraction, through to texture recognition. Lieshout [5] develops a point process for tracking rectangular objects from video. A mono-dimensional point process is proposed by Mallet *et al.* [6] for modeling 1D-signals by mixtures of parametric functions while imposing physical constraints between the modes.

1.2 Motivations

The results obtained by these point processes are particularly convincing and competitive, but the performances remain limited in terms of computation time and convergence stability, especially on large scenes. These drawbacks explain why industry has been reluctant until now to integrate these mathematical models in their products. Indeed, the point processes presented in Section 1.1 emphasize complex model formulations by proposing objects parametrically sophisticated [3, 4], advanced techniques to fit objects to the data [9], and non-trivial spatial interactions

between objects [6, 8]. However, these works have only slightly addressed the optimization issues from such complex models.

Jump-Diffusion algorithms [4, 12, 13] have been designed to speed-up the MCMC sampling by inserting diffusion dynamics for the exploration of the continuous subspaces. These samplers are unfortunately restricted to specific density forms. Data considerations have also been used to drive the sampling with more efficiency [14] for image segmentation problems. Some works have also proposed parallelization procedures by using multiple chains simultaneously [15] or decomposition schemes in configurations spaces of fixed dimension [16, 17]. However they are limited by border effects, and are not designed to perform on large scenes. In addition, the existing decomposition schemes cannot be used for configuration spaces of variable dimension. A mechanism based on multiple creation and destruction of objects has been also developed for addressing population counting problems [2, 9]. Nevertheless object creations require the discretization of the point coordinates which induces a significant loss of accuracy.

These alternative versions of the conventional MCMC sampler globally allow the improvement of optimization performances in specific contexts.That said, the gains in terms of computation time remain weak and are usually realized at the expense of solution stability. Finding a fast efficient sampler for general Markov point processes clearly represents a challenging problem.

1.3 Contributions

We present solutions to address this problem and to drastically reduce computation times while guarantying quality and stability of the solution. Our algorithm presents several important contributions to the field.

- **Sampling in parallel** - Contrary to the conventional MCMC sampler which makes the solution evolve by successive perturbations, our algorithm can perform a large number of perturbations simultaneously using a unique chain. The Markovian property of point processes is exploited to make the global sampling problem spatially independent in a neighborhood.

- **Non uniform point distributions** - Point processes mainly use uniform point distributions which are computationally easy to simulate, but make the sampling extremely slow. We propose an efficient mechanism allowing the modifications, creations or removals of objects by taking into account information on the observed scenes. Contrary to the data-driven solutions proposed by [3] and [14], our non-uniform distribution is not built directly from image likelihood, but is created via space-partitioning trees to ensure the sampling parallelization.

- **Efficient GPU implementation** - We propose an implementation on GPU which significantly reduces computing times with respect to existing algorithms, while increasing stability and improving the quality of the obtained solution.

- **3D object detection model from point cloud** - To evaluate the algorithm in 3D, we propose an original 3D point process to detect parametric objects from point clouds. This model is applied to tree recognition from laser scans of large urban and natural environments. To our knowledge, it is the first point process sampler to date to perform in such highly complex state spaces.

2 Point Process background

A point process describes random configurations of points in a continuous bounded set K. Mathematically speaking, a point process Z is a measurable mapping from a probability space $(\Omega, \mathcal{A}, \mathbb{P})$ to the set of configurations of points in K such that

$$\forall \omega \in \Omega, p_i \in K, Z(\omega) = \{p_1, ..., p_{n(\omega)}\} \tag{1}$$

where $n(\omega)$ is the number of points associated with the event ω. We denote by $\mathcal{P}$, the space of configurations of points in K. The most natural point process is the homogeneous Poisson process for which the number of points follows a discrete Poisson distribution whereas the position of the points is uniformly and independently distributed in K. Point processes can also provide more complex realizations of points by being specified by a density $h(.)$ defined in $\mathcal{P}$ and a reference measure $\mu(.)$ under the condition that the normalization constant of $h(.)$ is finite:

$$\int_{\boldsymbol{p} \in \mathcal{P}} h(\boldsymbol{p}) d\mu(\boldsymbol{p}) < \infty \tag{2}$$

The measure $\mu(.)$ having the density $h(.)$ is usually defined via the intensity measure $\nu(.)$ of an homogeneous Poisson process. Specifying a density $h(.)$ allows the insertion of data consistency, and also the creation of spatial interactions between the points. In particular, the Markovian property can be used in point processes, similarly to random fields, to create a spatial independence of the points in a neighborhood. Note also that $h(.)$ can be expressed by a Gibbs energy $U(.)$ such that

$$h(.) \propto \exp -U(.) \tag{3}$$

From points to parametric objects - What makes point processes attractive for vision is the possibility of marking each point p_i by additional parameters m_i such that the point becomes associated with an object $x_i = (p_i, m_i)$. We denote by $\mathcal{C}$, the corresponding space of object configurations where each configuration is given by $\boldsymbol{x} = \{x_1, ..., x_{n(\boldsymbol{x})}\}$. For example, a point process on $K \times M$ with $K \subset \mathbb{R}^2$ and the additional parameter space $M =]-\frac{\pi}{2}, \frac{\pi}{2}] \times [l_{min}, l_{max}]$ can be seen as random configurations of 2D line-segments since an orientation and a length are added to each point (see Fig. 1). Such point processes are also called marked point processes in the literature.

The most popular family of point processes corresponds to the Markov point processes of objects specified by Gibbs energies on $\mathcal{C}$ of the form

$$\forall \boldsymbol{x} \in \mathcal{C}, \;\; U(\boldsymbol{x}) = \sum_{x_i \in \boldsymbol{x}} D(x_i) + \sum_{x_i \sim x_j} V(x_i, x_j) \tag{4}$$

where $\sim$ denotes the symmetric neighborhood relationship of the Markov point process, $D(x_i)$ is a unitary data term measuring the quality of object x_i with respect to data, and $V(x_i, x_j)$, a pairwise interaction term between two neighboring objects x_i and x_j. The $\sim$relationship is usually defined via a limit distance ϵ between points such that

$$x_i \sim x_j = \{(x_i, x_j) \in \boldsymbol{x}^2 : i > j, ||p_i - p_j||_2 < \epsilon\} \tag{5}$$

In the sequel, we consider Markov point processes of this form. Note that this energy form has similarities with the standard labeling energies for MRFs. As detailed in Appendix D, our problem can be seen as a generalization of these models.

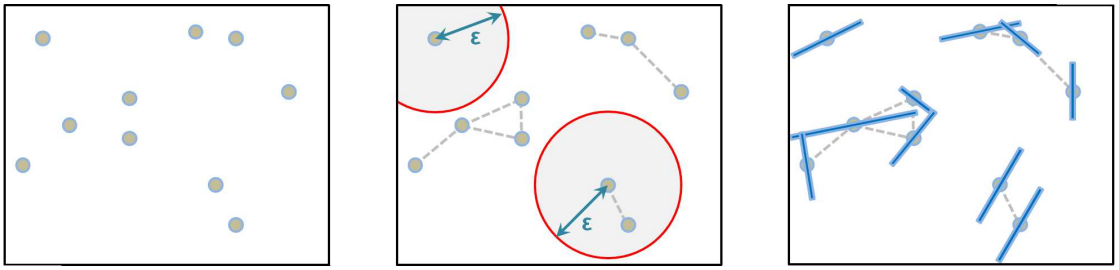

Figure 1: From left to right: realizations of a point process in 2D, of a Markov point process, and of a Markov point process of line-segments.The grey dashed lines represent the pairs of points interacting with respect to the neighboring relationship which is specified here by a limit distance ϵ between two points.

Simulation - Point processes are usually simulated by a Reversible Jump MCMC sampler [10] to search for the configuration which minimizes the energy U. This sampler consists of simulating a discrete Markov Chain $(X_t)_{t\in\mathbb{N}}$ on the configuration space $\mathcal{C}$, converging towards an invariant measure specified by U. At each iteration, the current configuration $\boldsymbol{x}$ of the chain is locally perturbed to a configuration $\boldsymbol{y}$ according to a density function $Q(\boldsymbol{x} \to .)$, also called a kernel. The perturbations are local, which means that $\boldsymbol{x}$ and $\boldsymbol{y}$ are close, and differ by no more than one object. The configuration $\boldsymbol{y}$ is then accepted as new state of the chain with a certain probability depending on the energy variation between $\boldsymbol{x}$ and $\boldsymbol{y}$, and a relaxation parameter T_t. The kernel Q can be formulated as a mixture of sub-kernels Q_m chosen with a probability q_m such that

$$Q(\boldsymbol{x} \to .) = \sum_m q_m Q_m(\boldsymbol{x} \to .) \tag{6}$$

Each sub-kernel is usually dedicated to specific types of moves, as the creation/removal of an object (Birth and Death kernel) or the modification of parameters of an object (*e.g.* translation, dilatation or rotation kernels). The kernel mixture must allow any configuration in $\mathcal{C}$ to be reached from any other configuration in a finite number of perturbations (irreductibility condition of the Markov chain), and each sub-kernel has to be reversible, *i.e.* able to propose the inverse perturbation.

The RJMCMC sampler is controlled by the relaxation parameter T_t, called the temperature, depending on time t and approaching zero as t tends to infinity. Although a logarithmic decrease of T_t is necessary to ensure the convergence to the global minimum from any initial configuration, one uses a faster geometric decrease which gives an approximate solution close to the optimum [1].

3 New sampling procedure

3.1 Simultaneous multiple perturbations

The conventional RJMCMC sampler performs successive perturbations on objects. Such a procedure is obviously long and fastidious, especially for large scale problems. A natural idea but still

Algorithm 1 RJMCMC sampler [10]

1- Initialize $X_0 = \boldsymbol{x}_0$ and T_0 at $t = 0$;
2- At iteration t, with $X_t = \boldsymbol{x}$,

- Choose a sub-kernel $\mathcal{Q}_m$ according to probability q_m
- Perturb $\boldsymbol{x}$ to $\boldsymbol{y}$ according to $Q_m(\boldsymbol{x} \to .)$
- Compute the Green ratio

$$R = \frac{\mathcal{Q}_m(\boldsymbol{y} \to \boldsymbol{x})}{\mathcal{Q}_m(\boldsymbol{x} \to \boldsymbol{y})} \exp\left(\frac{U(\boldsymbol{x}) - U(\boldsymbol{y})}{T_t}\right) \tag{7}$$

- Choose $X_{t+1} = \boldsymbol{y}$ with probability $\min(1, R)$, and $X_{t+1} = \boldsymbol{x}$ otherwise

unexplored for Markov point processes consists in sampling objects in parallel by exploiting their conditional independence outside the local neighborhood. Such a strategy implies partitioning the space K so that simultaneous perturbations are performed at locations far enough apart to not interfere and break the convergence properties.

From sequential to parallel sampling - Let $(X_t)_{t\in\mathbb{N}}$, be a Markov chain simulating a Markov point process in K using a MCMC dynamics, and $\{c_s\}$ be a partition of the space K, where each component c_s is called a cell. Two cells c_1 and c_2 are said *independent on* X if the transition probability for any random perturbation falling in c_1 and at any time t does not depend on either objects or perturbations falling in c_2, and vice versa.

We can demonstrate that the transition probability of two successive perturbations falling in independent cells under the temperature T_t is equal to the product of the transition probabilities of each perturbation under the same temperature. In other words, realizing two successive perturbations on independent cells at the same temperature is equivalent to performing them in parallel.

Let $\boldsymbol{x}$, be a realization of the point process such that $\boldsymbol{x} = (x_1, x_2, u)$ where x_1 (respectively x_2) represents the set of points falling in the cell c_1 (respectively c_2), and u is the remaining set of points falling in $K - \{c_1, c_2\}$. Let $\boldsymbol{y}$, be a new configuration of points obtained from $\boldsymbol{x}$ by two perturbations on the cells c_1 and c_2 so that we have $\boldsymbol{y} = (y_1, y_2, u)$. The probability $\Pr[X_{t+2} = \boldsymbol{y} | X_t = \boldsymbol{x}]$ can be expressed as

$$\begin{aligned} &\Pr[X_{t+2} = \boldsymbol{y} | X_t = \boldsymbol{x}] = \\ &\Pr[X_{t+2} = (y_1, y_2, u) | X_{t+1} = (y_1, x_2, u)] \times \Pr[X_{t+1} = (y_1, x_2, u) | X_t = \boldsymbol{x}] \\ &+ \Pr[X_{t+2} = (y_1, y_2, u) | X_{t+1} = (x_1, y_2, u)] \times \Pr[X_{t+1} = (x_1, y_2, u) | X_t = \boldsymbol{x}] \end{aligned} \tag{8}$$

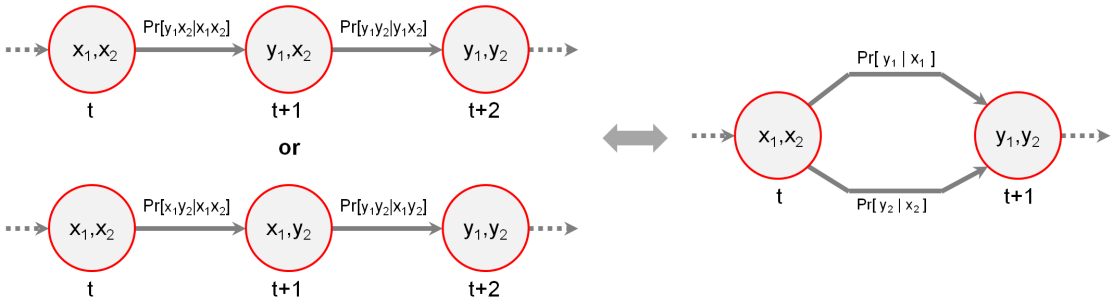

Figure 2: Illustration of the equivalence between two successive perturbations on independent cells c_1 and c_2, and two simultaneous perturbations on each cell.

or, as the temperature parameter is constant between t and $t+2$, we have

$$\begin{aligned}
&\Pr[X_{t+2} = \boldsymbol{y} | X_{t+1}] = (y_1, x_2, u) \\
&= Q((y_1, x_2, u) \to \boldsymbol{y}) \times \min\left[1, \tfrac{\mathcal{Q}(\boldsymbol{y} \to (y_1, x_2, u))}{\mathcal{Q}((y_1, x_2, u) \to \boldsymbol{y})} \exp\left(\tfrac{U((y_1, x_2, u)) - U(\boldsymbol{y})}{T_{t+1}}\right)\right] \\
&= Q((y_1, x_2, u) \to \boldsymbol{y}) \times \min\left[1, \tfrac{\mathcal{Q}(\boldsymbol{y} \to (y_1, x_2, u))}{\mathcal{Q}((y_1, x_2, u) \to \boldsymbol{y})} \exp\left(\tfrac{U((y_1, x_2, u)) - U(\boldsymbol{y})}{T_t}\right)\right] \\
&= \Pr[X_{t+1} = \boldsymbol{y} | X_t = (y_1, x_2, u)]
\end{aligned} \tag{9}$$

The cells c_1 and c_2 being independent, the transition probability for the perturbation y_2 falling in c_2 does not depend, by definition, on x_1 and y_1. Thus we have in particular

$$\Pr[X_{t+1} = (y_1, y_2, u) | X_t = (y_1, x_2, u)] = \Pr[X_{t+1} = (x_1, y_2, u) | X_t = (x_1, x_2, u)] \tag{10}$$

we obtain

$$\Pr[X_{t+2} = \boldsymbol{y} | X_{t+1} = (y_1, x_2, u)] = \Pr[X_{t+1} = (x_1, y_2, u) | X_t = \boldsymbol{x}] \tag{11}$$

Similarly, we can demonstrate that

$$\Pr[X_{t+2} = \boldsymbol{y} | X_{t+1} = (x_1, y_2, u)] = \Pr[X_{t+1} = (y_1, x_2, u) | X_t = \boldsymbol{x}] \tag{12}$$

Finally, by inserting Eq. 11 and 12 in Eq. 8, we obtain the expected result

$$\begin{aligned}
&\Pr[X_{t+2} = \boldsymbol{y} | X_t = \boldsymbol{x}] = \\
&2! \Pr[X_{t+1} = (y_1, x_2, u) | X_t = \boldsymbol{x}] \times \Pr[X_{t+1} = (x_1, y_2, u) | X_t = \boldsymbol{x}]
\end{aligned} \tag{13}$$

where 2! is the combinatorial coefficient corresponding to the number of permutations of perturbations in the sequential chain.

Ensuring cell independence - Two independent cells must be located at a minimum distance from each other. As illustrated in Fig. 3, this distance must take into account both the

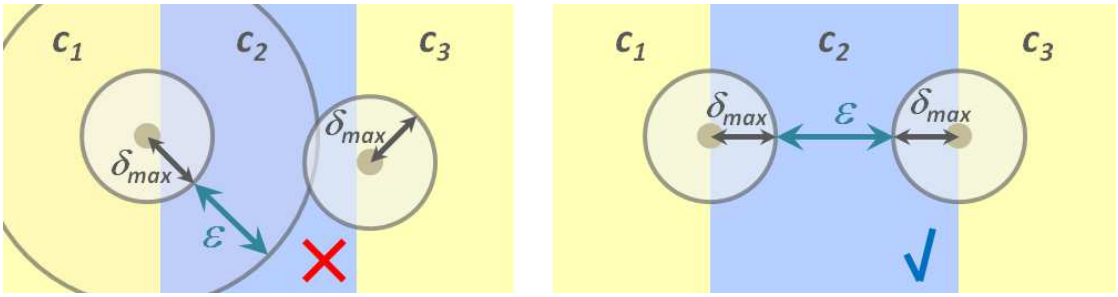

Figure 3: Independence of cells. On the left case, the width of the cell c_2 is not large enough to ensure the independence of the cells c_1 and c_3: the two grey points in c_1 and c_3 cannot be perturbed at the same time. On the right case, the cells c_1 and c_3 are independent as Eq. 14 is satisfied.

width of the neighboring relationship, *i.e.* ϵ, and the length of the biggest move allowed as object perturbation, denoted by $\delta_{\max}$. Independence between two cells c_s and $c_{s'}$ is then guaranteed if

$$\min_{p \in c_s,\, p' \in c_{s'}} ||p - p'||_2 \geq \epsilon + 2\delta_{\max} \tag{14}$$

Independent cell gathering - The natural idea consists of partitioning the space K into a regular mosaic of cells with size greater than or equal to $\epsilon + 2\delta_{\max}$. The cells can then be regrouped into $2^{\dim K}$ sets such that each cell is adjacent to cells belonging to different sets. Fig. 4 illustrates the regrouping scheme for $\dim K = 2$ and $\dim K = 3$. This regrouping scheme ensures the mutual independence between all the cells of a same set. In the sequel, such a set is called a *mic-set* (set of Mutually Independent Cells).

3.2 Non-uniform point distributions

Sampling objects in parallel via a regular partitioning, as illustrated on Fig. 3- (c)&(d), is however not optimal because the spatial point distribution is necessarily uniform and does not take into account the characteristics of observed scenes. To overcome this problem, a non-regular partitioning of the scene is created by exploiting data-based knowledge.

Non-uniform kernel from uniform sub-kernels - Mixtures of sub-kernels are frequently used to simulate point processes by MCMC dynamics, each sub-kernel corresponding to a perturbation type (*e.g.* birth and death, translation, rotation, etc). However, the idea consisting of accumulating sub-kernels with spatial restrictions to create non-uniform point distributions has not been exploited in the literature. Let $\{c_s\}^{(1)}, .., \{c_s\}^{(L)}$, be L partitions of the space K such that $\{c_s\}^{(i)}$ is a subdivided partition of $\{c_s\}^{(i-1)}$. The L partitions define a space-partitioning tree, denoted $\mathcal{K}$ and whose levels each correspond to a partition of K. By associating with each cell contained in $\mathcal{K}$ a uniform sub-kernel spatially restricted to the subspace supporting this cell, a non-uniform kernel can be created by accumulation, as defined in Eq. 6 and illustrated in Fig. 5.

Data-driven space-partitioning tree - A regular 1-to-$2^{\dim K}$ hierarchical subdivision scheme is considered to build a partitioning tree, typically a quadtree in dimension two and an octree in

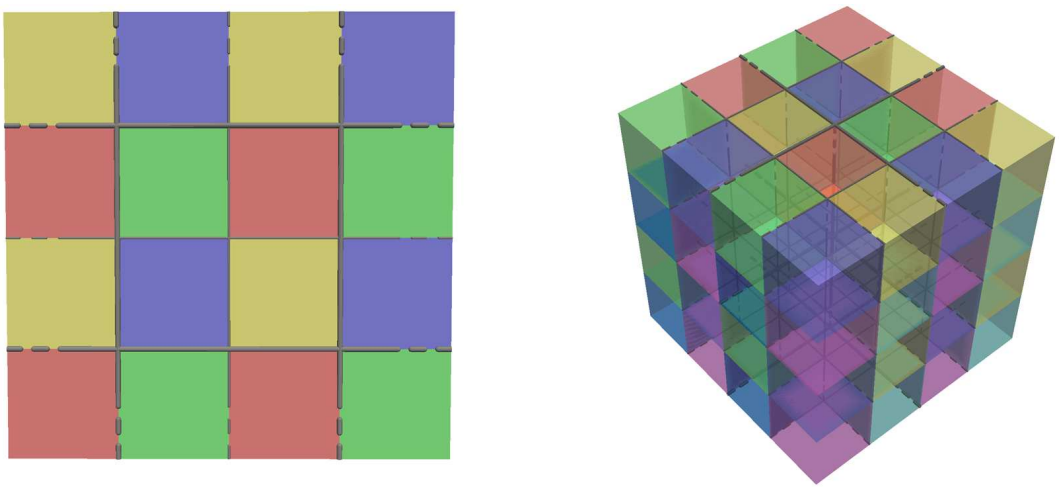

Figure 4: Trivial partitioning scheme of K. In dimension two (left), the cells are squares regrouped into 4 mic-sets (yellow, blue, red and green). Each cell is adjacent to cells belonging to different mic-sets. In dimension three (right), the cells are cubes regrouped into 8 mic-sets.

dimension three. The subdivision of the cells is driven by the data. We assume that a class of interest in K, in which the objects have a high probability to belong to, can be roughly distinguished from the data. The extraction of such a class is not addressed here, and is supposed to be done by a segmentation algorithm of the literature adapted to the considered application. A cell at a given level of the tree is divided into $2^{\dim K}$ cells at the next level if it overlaps with the given class of interest. The hierarchical decomposition is stopped when the minimal size of the cell becomes inferior to $\epsilon+2\delta_{\max}$, *i.e.* when the cell independence condition (Eq. 14) is not longer valid.

The partitioning tree allows the creation of a non uniform point distribution naturally and efficiently. Indeed, the density progressively decreases when moving far from the class of interest as shown in Fig. 5, while being ensured to be non-null. The point distribution is thus not directly affected when the class of interest is inaccurately extracted.

Kernel formulation - Given a space-partitioning tree $\mathcal{K}$ composed of L levels, and $2^{\dim K}$ mic-sets for each level, we can formulate a general kernel Q as a mixture of uniform sub-kernels $Q_{c,t}$, each sub-kernel being defined on the cell c of $\mathcal{K}$, by the perturbation type $t \in \mathcal{T}$, such that

$$\forall \boldsymbol{x} \in \mathcal{C},\ Q(\boldsymbol{x} \to .) = \sum_{c \in \mathcal{K}} \sum_{t \in \mathcal{T}} q_{c,t}\, Q_{c,t}(\boldsymbol{x} \to .) \tag{15}$$

where $q_{c,t}$ is the probability of choosing sub-kernel $Q_{c,t}(\boldsymbol{x} \to .)$, given by

$$q_{c,t} = \frac{\Pr(t)}{\#\text{cells in } \mathcal{K}} \tag{16}$$

Four types of kernels are usually considered in practice so that we have $\mathcal{T} = \{$birth and death, translation, rotation, scale$\}$. The switching kernel can also be used when objects have several possible types. Note that the kernel Q is reversible as a sum of reversible sub-kernels. Note also

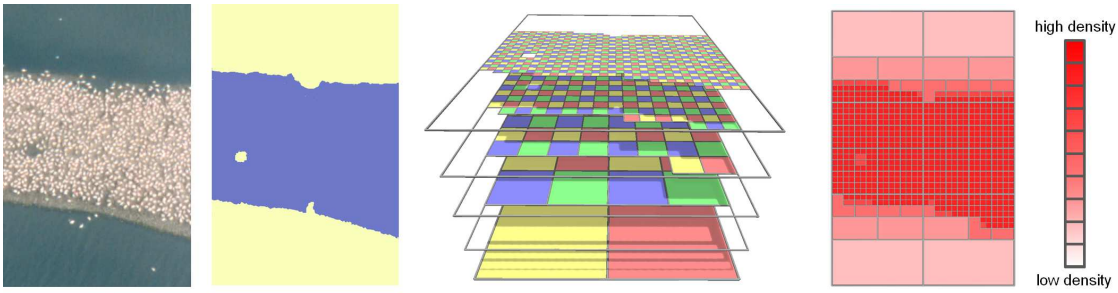

Figure 5: Space partitioning tree in dimension two. (b) A class of interest (blue area) is estimated from (a) an input image. (c) A quadtree is created so that the levels are recursively partitioned according to the class of interest. Each level is composed of four mic-sets (yellow, blue, red and green sets of cells) to guaranty the sampling parallelization. (d) The cell accumulation at the different levels designs a non uniform distribution. Note how the distribution naturally describes the class of interest by progressively decreasing the density when moving away.

that this kernel allows us to visit the whole configuration space $\mathcal{C}$ since it is guaranteed by the sub-kernels of the coarsest level of $\mathcal{K}$.

3.3 Sampler formulation

The kernel defined in Eq. 15 is embedded into the MCMC dynamics so that the new sampler allows the association of multiple perturbations performed in parallel with relevant non-uniform point distributions based on data-driven space partitioning trees. Algorithm 2 details the sampling procedure.

Algorithm 2 Our parallel sampler

1-Initialize $X_0 = \boldsymbol{x}_0$ and T_0 at $t = 0$;
2-Compute a space-partitioning tree $\mathcal{K}$;
3-At iteration t, with $X_t = \boldsymbol{x}$,

- Choose a mic-set $S_{mic} \in \mathcal{K}$ and a kernel type $t \in \mathcal{T}$ according to probability $\sum_{c \in S_{mic}} q_{c,t}$
- For each cell $c \in S_{mic}$,
  - Perturb $\boldsymbol{x}$ in the cell c to a configuration $\boldsymbol{y}$ according to $Q_{c,t}(\boldsymbol{x} \to .)$
  - Calculate the Green ratio

$$R = \frac{\mathcal{Q}_{c,t}(\boldsymbol{y} \to \boldsymbol{x})}{\mathcal{Q}_{c,t}(\boldsymbol{x} \to \boldsymbol{y})} \exp\left(\frac{U(\boldsymbol{x}) - U(\boldsymbol{y})}{T_t}\right) \tag{17}$$

  - Choose $X_{t+1} = \boldsymbol{y}$ with probability $\min(1, R)$, and $X_{t+1} = \boldsymbol{x}$ otherwise

Note that the temperature parameter is updated after each series of simultaneous perturbations such that the temperature decrease is equivalent to a cooling schedule by plateau in a standard

sequential MCMC sampling. Note also that the hierarchical partitioning of K protects the sample from mosaic effects. In practice, the sampling is stopped when no perturbation has been accepted during a certain number of iterations.

4 Experiments

The proposed algorithm has been implemented on GPU for $\dim K = 2$ and $\dim K = 3$, and tested on various problems including population counting, line-network extraction from images, and object recognition from 3D point clouds. Note that additional results and comparisons are given in 5, as well as details on energy formulations.

4.1 Implementation

The algorithm has been implemented on GPU using CUDA. A thread is dedicated to each simultaneous perturbation so that operations are performed in parallel for each cell of a mic-set. The sampler is thus all the more efficient as the mic-set contains many cells, and generally speaking, as the scene supported by K is large. Moreover, the code has been programmed to avoid time-consuming operations. In particular, the threads do not communicate between each other, and memory coalescing permits fast memory access. The memory transfer between CPU and GPU has also been minimized by indexing the parametric objects. The experiments presented in this section have been performed on a 2.5 Ghz Xeon computer with a Nvidia graphics card (Quadro 4800, architecture 1.3).

4.2 Point processes in 2D

The algorithm has been evaluated on population counting problems from large-scale images using a point process in 2D, *i.e.* with $\dim K = 2$. The problem presented in Fig. 6 consists in detecting migrating birds to extract information on their number, their size and their spatial organization. The point process is marked by ellipses which are simple geometric objects defined by a point (center of mass) and 3 additional parameters, and are well adapted to capture the bird contours. The energy is specified by a unitary data term based on the Bhattacharyya distance between the radiometry inside and outside of the object, and a pairwise interaction penalizing the strong overlapping of objects (see Appendix A).

Computation time, quality of the reached energy, and stability are the three important criteria used to evaluate and compare the performance of samplers. As shown on Fig. 7, our algorithm obtains the best results for each of the criteria compared to the existing samplers. In particular, we reach a better energy (-8.76 *vs* -5.78 for [2] and -2.01 for [10]) while significantly reducing computation times (269 sec *vs* 1078 sec for [2] and 2.8×10^6 sec for [10]). Note that, for the reasons mentioned in Section 4.1, this gap in performance increases when the input scene becomes larger. Fig. 7 also underlines an important limitation of the reference point process sampler for population counting [2] compared to our algorithm. Indeed, the discretization of the object parameters required in [2] causes approximate detection and localization of objects which explains the average quality of the reached energy. The stability is analyzed by the coefficient of variation, defined as the standard deviation over mean and known to be a relevant statistical measure for comparing methods having different means. Our sampler provides a better stability than the existing algorithms.

The impact of the data-driven space partitioning tree is also measured by performing tests with

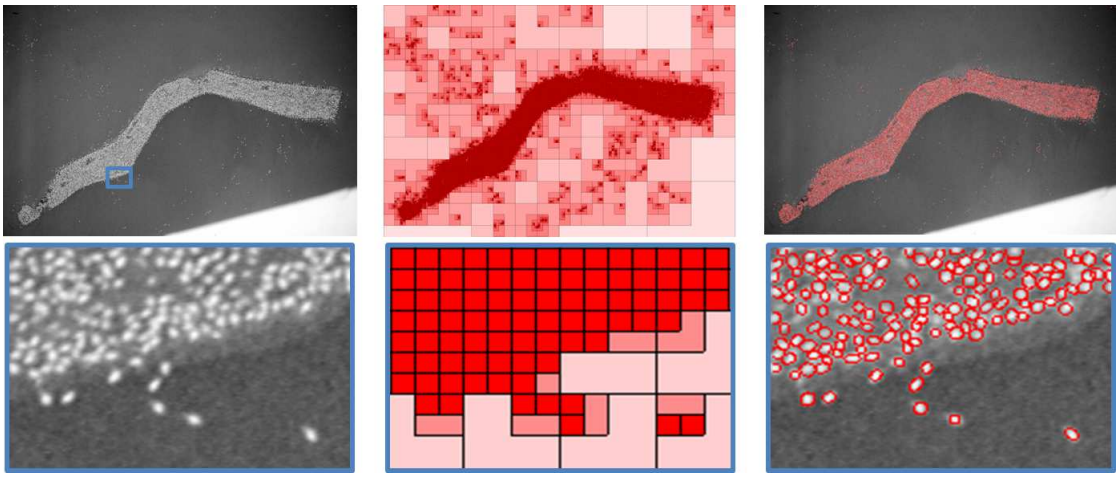

Figure 6: Bird counting by a point process of ellipses. (right) More than ten thousand birds are extracted by our algorithm in a few minutes from (left) a large scale aerial image. (middle) A quad-tree structure is used to create a non-uniform point distribution. Note, on the cropped parts, how the birds are accurately captured by ellipses in spite of the low quality of the image and the partial overlapping of birds.

	Coefficient of variation		
	energy	time	#objects
RJMCMC [10]	7.3%	4.2%	1.7%
multiple birth and death [2]	5.0%	2.1%	1.3%
our sampler without partitioning tree	7.4%	6.2%	1.6%
our sampler with partitioning tree	4.4%	1.8%	1.1%

Table 1: Performances of the various samplers. The table presents the coefficients of variation of the energy, time and number of objects reached at the convergence over 50 simulations.

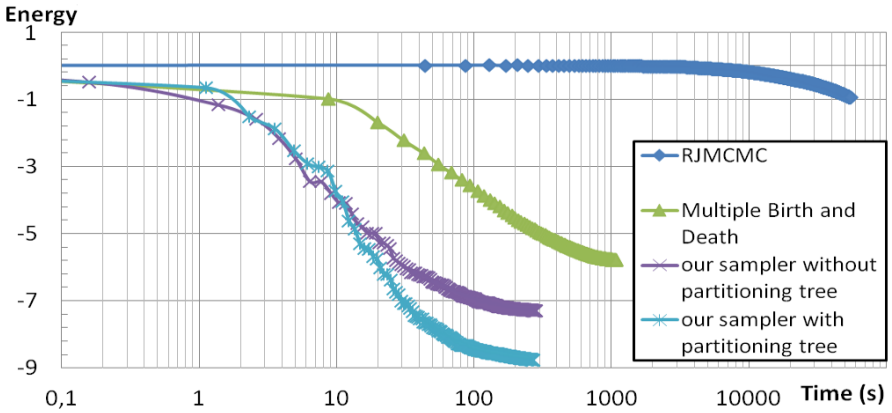

Figure 7: Performances of the various samplers. The graph describes the energy decrease over time from the bird image presented in Fig. 6. Time is represented using a logarithmic scale. Note that the RJMCMC algorithm [10] is so slow that the convergence is not displayed on the graph (2.9×10^7 iterations are required versus 1.8×10^4 for our algorithm).

	our sampler	Jump-Diffusion [4]	RJMCMC [7]	Active contour [18]
Time (minute)	0.26	6.35	155	60
Over-detection	0.45%	2.06%	0.06%	2.28%
Under-detection	32.7%	52.7%	17%	58.9%
Representation	line-segment	line-segment	line-segment	pixels

Table 2: Comparisons with existing line-network extraction methods from the image presented in Fig. 8.

uniform point distributions. The performances decrease but remain better than the existing algorithms. In particular, the sampler loses stability, and the objects are detected and located less accurately than with the partitioning tree.

The algorithm has also been tested on line-network extraction from images. The parametric objects here are line-segments defined by a point (center of mass) and two additional parameters (length and orientation). Contrary to the population counting model, the pairwise potential includes a connexion interaction for linking the line-segments. Figure 8 shows a road network extraction result obtained from a satellite image whereas Table 2 provides elements of comparisons with existing methods. The result quality in terms of road under/over-detection is globally similar to existing approaches (higher than [4] and [18], and lower than [7]), but our algorithm significantly improves the computing times. 16 seconds are required in our case, compared to 7 minutes by a Jump-Diffusion algorithm [4], 155 minutes for a RJMCMC method [7], and 60 minutes for an Active Contour based approach [18].

4.3 Point processes in 3D

We tested our algorithm with $\dim K = 3$ on an original object recognition problem from laser scans. The goal is to extract trees from unstructured point clouds containing a lot of outliers, noise and other different objects (buildings, ground, cars, fences, wires, *etc*), and to recognize

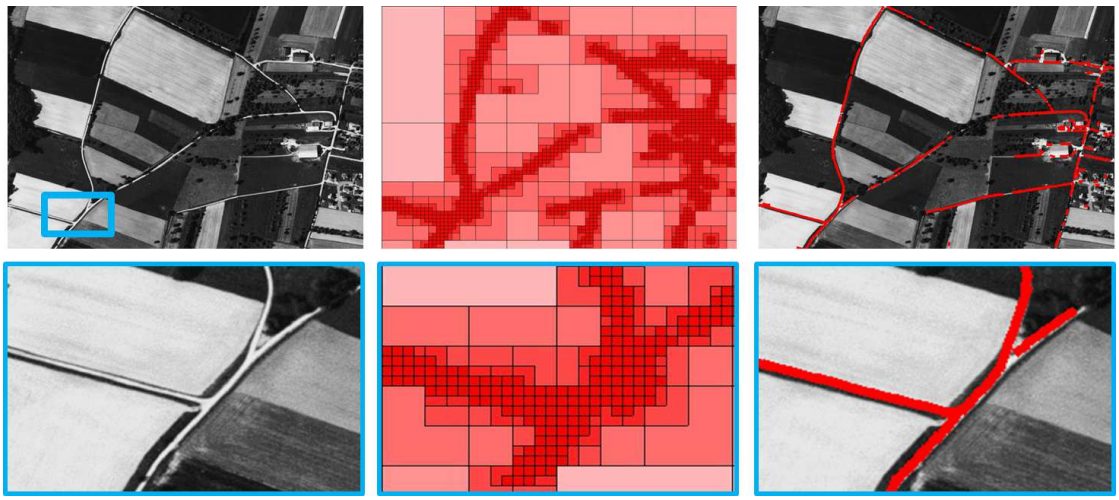

Figure 8: Line-network extraction by a point process of line-segments. (middle) Even if the point distribution is roughly estimated, (right) the road network is recovered (red segments) by our algorithm in 16 seconds from (left) a satellite image. Note that, as shown on the close-up, some parts of the network can be omitted when roads are hidden by trees at some locations: existing methods also encounter difficulties in such cases.

their shapes and types. The objects associated with the point process correspond to a library of different 3D-templates of trees detailed in Appendix C. The unitary data term of the energy measures the distance from points to a 3D-template, whereas the pairwise interaction takes into account constraints on object overlapping as well as on tree type competition. Compared to the former applications, the configuration space $\mathcal{C}$ is of higher dimension since the objects are parametrically more complex. This allows our algorithm to exploit more deeply its potential. The rotation kernel is not used here since the objects are invariant by rotation. However, we use a switching kernel in order to exchange the type of an object.

Fig. 9 shows results obtained from laser scans of large urban and natural environments. 30 (respectively 5.4) thousand trees are extracted in 96 (resp. 53) minutes on the 3.7km^2 mountain area (resp. 1km^2 urban area) from 13.8 (resp. 2.3) million input points. The computation times can appear high, but finding non-trivial 3D-objects in such larges scenes by point processes is a challenge which, to our knowledge, has not been achieved until now due to the extreme complexity of the state space. Note also that the performances could be improved by reducing the space $\mathcal{C}$ with a 3D-point process on manifolds, *i.e.* where the z-coordinate of points is determined by an estimated ground surface.

Evaluating the detection quality with accuracy for this application is a difficult task since no ground truth exists. As illustrated on the cropped part in Fig. 9, we have manually indexed the trees on different zones from aerial images acquired with the laser scans. The objects are globally well located and fitted to the input points with few omissions, even when trees are surrounded by other types of urban entities such as buildings. The non-overlapping constraint of the energy allows us to obtain satisfactory results for areas with high tree density. Errors frequently occur

in distinguishing the tree type in spite of the tree competition term of the energy.

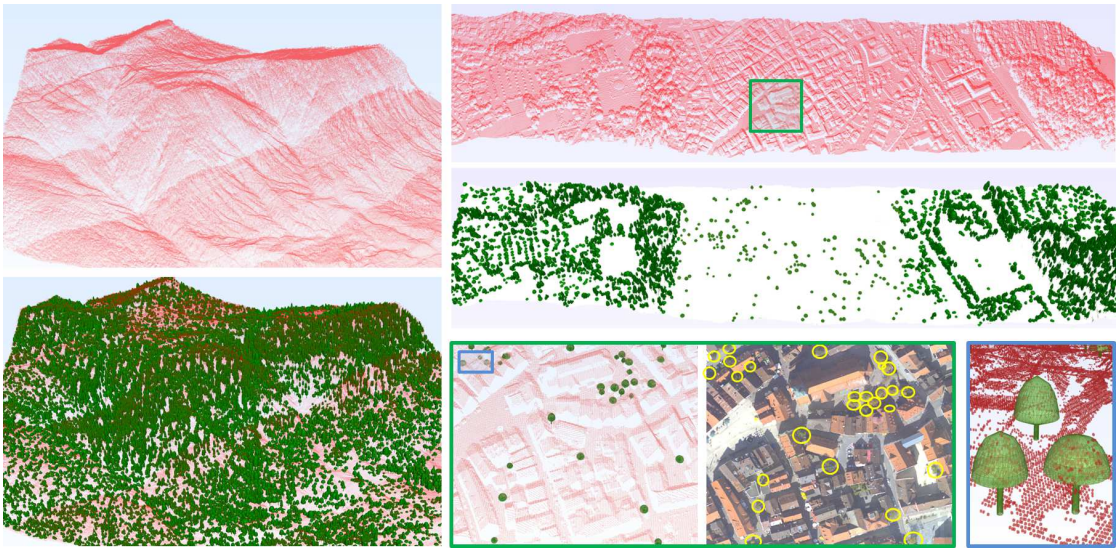

Figure 9: Tree recognition from point clouds by a 3D-point process specified by 3D-parametric models of trees. Our algorithm detects trees and recognizes their shapes in large-scale (left, input scan: 13.8M points) natural and (top right, input scan: 2.3M points) urban environments, in spite of other types of urban entities, e.g. buildings, car and fences, contained in input point clouds (red dot scans). An aerial image is joined to (bottom right) the cropped part to provide a more intuitive representation of the scene and the tree location. Note, on the cropped part, how the parametric models fit well to the input points corresponding to trees, and how the interaction of tree competition allows the regularization of the tree type in a neighborhood.

5 Conclusion

We propose a new algorithm to sample point processes whose strengths lean on the exploitation of Markovian properties to enable the sampling to be performed in parallel, and the integration of a data-driven mechanism allowing efficient distributions of the points in the scene. Our algorithm improves the performances of the existing samplers in terms of computing times and stability, especially on large scenes where the gain is very important. It can be used without particular restrictions, contrary to most samplers, and even appears as an interesting alternative to the standard optimization techniques for MRF labeling problems as explained in Appendix D. In particular, one can envisage using the model proposed in Section 4.3 to extract any type of parametric objects from large 3D-point clouds. In future works, it would be interesting to implement the algorithm on other GPU architectures more adapted to the manipulation of 3D data structures, *e.g.* architecture 2.0, so that the performances for point processes in 3D could be improved.

Acknowledgments.

This work was partially funded by the European Research Council (ERC Starting Grant "Robust Geometry Processing", Grant agreement 257474). The authors thank A. Lehmussola, H. Bischof, the French Mapping Agency (IGN), the Tour du Valat, and the BRGM for provinding the datasets.

Appendices

A Details on the population counting model from images

In this appendix, we detail the energy model used for the 2D-point process of ellipses that has been presented in section 4.2 of the paper. x represents a configuration of ellipses. The center of mass p of an ellipse is contained in the compact set K supporting the data image (see Fig. 10).

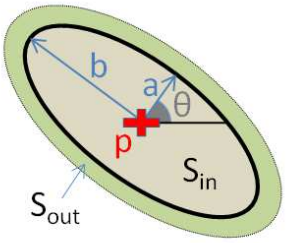

Figure 10: Ellipse parameters: an ellipse is defined by a point $p \in K$ (center of mass of the object) and 3 additional parameters which are the semi-major axis b, the semi-minor axis a, and the angle θ. The inside (respectively bordering) volume of the object is denoted by S_{in} (respectively S_{out}).

The energy follows the form given by Eq. 4 of the paper:

$$U(x) = \sum_{x_i \in \boldsymbol{x}} D(x_i) + \sum_{x_i \sim x_j} V(x_i, x_j) \tag{18}$$

where the unitary data term $D(x_i)$ and the potential $V(x_i, x_j)$ are given by:

$$D(x_i) = \begin{cases} 1 - \frac{d(x_i)}{d_0} & \text{if } d(x_i) < d_0 \\ exp(\frac{d_0 - d(x_i)}{d_0}) - 1 & \text{otherwise} \end{cases} \tag{19}$$

$$V(x_i, x_j) = \beta \frac{A(x_i \cap x_j)}{\min(A(x_i), A(x_j))} \tag{20}$$

- $d(x_i)$ represents the Bhattacharyya distance between the radiometry inside and outside the object x_i:

$$d(x_i) = \frac{m_{in}^2 - m_{out}^2}{4(\sigma_{in} - \sigma_{out})} - \frac{1}{2} ln(\frac{2\sigma_{in}\sigma_{out}}{\sigma_{in}^2 + \sigma_{out}^2}) \tag{21}$$

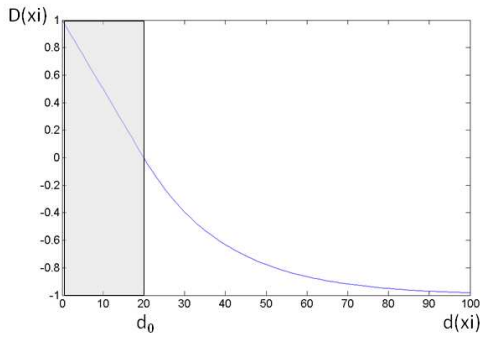

Figure 11: Data term $D(x_i)$ in function of the Bhattacharyya distance $d(x_i)$. The higher the coefficient d_0, the more selective the object fitting.

where m_{in} and σ_{in} (respectively m_{out} and σ_{out}) are the intensity mean and standard deviation in S_{in} (respectively in S_{out}).

- d_0 is a coefficient fixing the sensitivity of the object fitting.
- $A(x_i)$ is the area of object x_i.
- β is a coefficient weighting the non-overlapping constraint with respect to the data term

Figures 12 and 13 describe the evolution of the objects during the sampling in case of bird counting. Note that a basic mathematical dilatation is used to roughly extract the class of interest from the image of birds (see Fig. 12-(b)).

B Details on the line-network extraction model from images

We detail here the energy model used for the 2D-point process of line-segments that has been presented in section 4.2 of the paper. The model formulation is relatively similar to the population counting problem detailed in Appendix 2. As illustrated on Fig. 14, a line-segment is defined by five parameters, including the 2D point corresponding to the center of mass of the object.
Similarly to the population counting model, the fitting quality with respect to the data is based on the Bhattacharyya distance. The unitary data term $D(x_i)$ of the energy is given by Eq. 19. The potential $V(x_i, x_j)$ penalizes strong object overlaps (see Eq. 20). However the potential also takes into account a connection interaction in order to favor the linking of the line-segments. The potential term is given by:

$$V(x_i, x_j) = \beta_1 \frac{A(x_i \cap x_j)}{\min(A(x_i), A(x_j))} + \mathbf{1}_{x_i \sim_{nc} x_j} \times \beta_2 f(x_i, x_j) \tag{22}$$

- β_1 and β_2 are two coefficient weighting respectively the non-overlapping and connection constraints with respect to the data term.
- $\sim_{nc}$ is the non-connection relationship between two objects. $x_i \sim_{nc} x_j$ if the anchor areas of x_i and x_j (see Fig. 14) do not overlap.

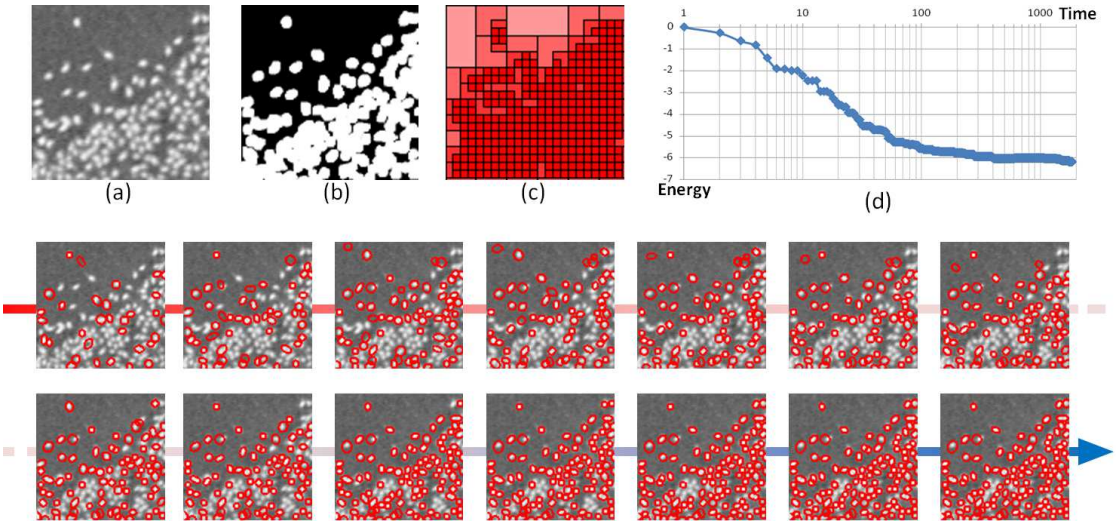

Figure 12: Evolution of the object configuration during the sampling. (a) An image path representing a bird population is roughly segmented by mathematical dilatation into a (b) binary image (white color corresponds to the class of interest). (c) A quadtree is created from the segmented image. (d) Energy progressively decreases during the sampling while (bottom) the objects in the current configuration become more and more relevant.

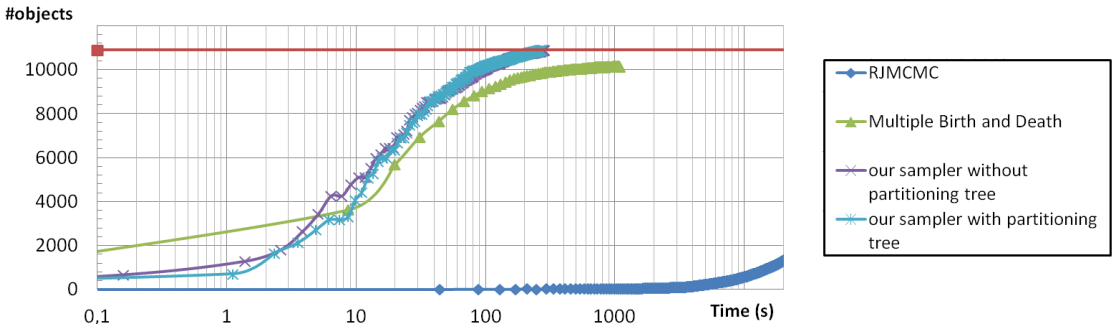

Figure 13: Evolution of the number of objects during the sampling from the bird image presented in Fig. 4 of the paper. Note that time is represented using a logarithmic scale, and that RJMCMC algorithm [10] is so slow that the convergence is not displayed on the graph. The red line indicates the number of birds found by an expert (ground truth). The number of objects found by our sampler is very close to the expert number, which is not the case of the other samplers. Note that estimating the correct number of object does not mean that the objects are correctly fitted to the data, but it is an important criterion for population counting problems as mentioned in [19].

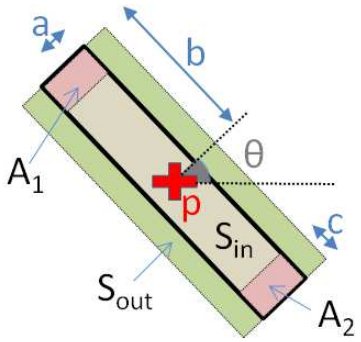

Figure 14: Line-segment parameters. A line-segment is defined by a point $p \in K$ (center of mass of the object) and 3 additional parameters which are the semi-length b, the semi-width a, and the orientation θ. Note that the semi-width a can be preliminarily fixed depending on the application, e.g. for mono-scale road-network extraction. The inside (respectively bordering) volume of the object is denoted by S_{in} (respectively S_{out}). The length of the connection area c, also called the anchor area, is a parameter of the model formulation. The anchors are denoted by A_1 and A_2.

- $\mathbf{1}_{condition}$ is the indicative function returning one when *condition* is valid, and zero otherwise.

- $f(x_i, x_j)$ is a symmetric function weighting the penalization of two non-connected objects x_i and x_j with respect to their average fitting quality. The function f is introduced to slightly relax the connection constraint when the two objects are of very good quality.

As for the bird counting problem, we use a basic mathematical dilatation to roughly extract the class of interest from the aerial image of road-network shown on Figure 6 of the paper. Indeed the road pixels in this image are relatively bright compared to the background. The segmented result is definitively not optimal, but sufficient to create an efficient partitioning tree (see Figure 6 -(middle) of the paper).

C Details on the tree recognition model from 3D point clouds

In this appendix, we detail the energy model used for the 3D-point process of trees that has been presented in section 4.3 of the paper. x represents a configuration of 3D-models of trees from a template library described in Fig. 15.
The center of mass p of a tree is contained in the compact set K supporting the 3D bounding box of the input point cloud (see Fig. 16). We denote by ∂x_i the surface of the object x_i, and by $\mathcal{C}x_i$ the cylindrical volume having a vertical axis passing through the center of mass of x_i, in which the input points are considered to measure the quality of x_i.
The energy follows the form given by Eq. 4 of the paper with the unitary data term $D(x_i)$ and

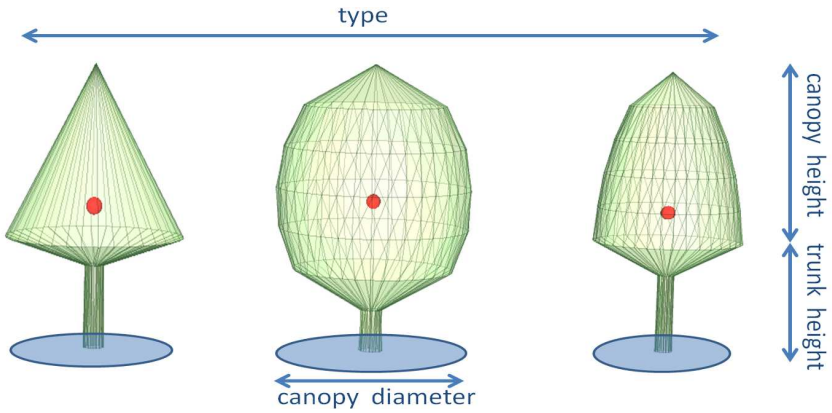

Figure 15: Library of tree models - the objects are specifyed by a 3D point (center of mass illustrated by a red dot) and additional parameters (blue arrows) including the canopy type whose shape can be conoidal (*e.g.* pine or fir), ellipsoidal (*e.g.* poplar or tilia) or semi-ellipsoidal (*e.g.* oak or maple).

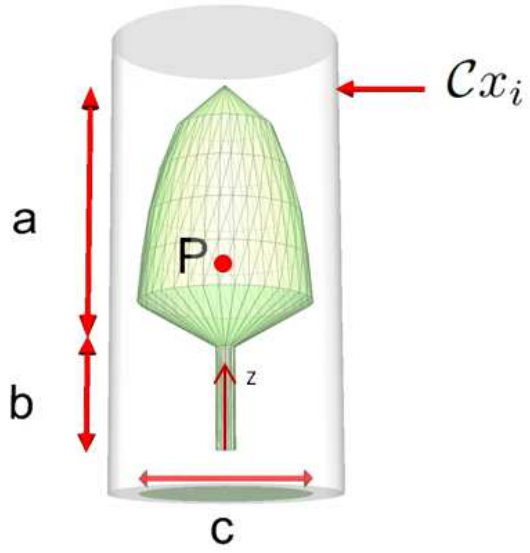

Figure 16: Tree parameters - a tree is defined by a point $p \in K$ (center of mass of the object), a type $t \in \{$conoidal, ellipsoidal, semi-ellipsoidal$\}$, and 3 additional parameters which are the canopy height a, the trunk height b and the canopy diameter c. The cylindrical volume $\mathcal{C}x_i$ represents the attraction space of object x_i in which the input points are used to measure the quality of this object.

the pairwise potential $V(x_i, x_j)$ given by:

$$D(x_i) = \frac{1}{|\mathcal{C}x_i|} \prod_{p_c \in \mathcal{C}x_i} \gamma(d(p_c, \partial x_i)) \tag{23}$$

$$V(x_i, x_j) = \beta_1 V_{overlapping}(x_i, x_j) + \beta_2 V_{competition}(x_i, x_j) \tag{24}$$

- $|\mathcal{C}x_i|$ is a coefficient normalizing the unitary data term with respect to the number of input points contained in $\mathcal{C}x_i$.
- $d(p_c, \partial x_i)$ is a distance measuring the coherence of the point p_c with respect to the object surface ∂x_i. d is not the conventional orthogonal distance from point to surface because, as real trees do not describe ellipsoidal/conoidal shapes, input points are not homogeneously distributed on the object surface. Here, d is defined as the combination of the planimetric distance, *i.e.* the projection in the plane of equation $z = 0$ of the Euclidean distance, and the altimetric variation such that points outside the object are more penalized than inside points. Fig. 17 illustrates the behavior of d in the XZ-plane. Note that d is invariant by rotation around Z-axis.
- $\gamma(.) \in [-1, 1]$ is a quality function which is strictly increasing.
- $V_{overlapping}$ is the pairwise potential penalizing strong overlapping between two objects, and given by:

  $$V_{overlapping}(x_i, x_j) = \frac{A(x_i \cap x_j)}{\min(A(x_i), A(x_j))} \tag{25}$$

  where $A(x_i)$ is the area of the object x_i projected onto the plane of equation $z = 0$.
- $V_{competition}$ is the pairwise potential favoring similar tree type t in a neighborhood:

  $$V_{competition}(x_i, x_j) = \mathbf{1}_{t_i \neq t_j} \tag{26}$$

  where $\mathbf{1}_.$ is the indicative function.
- β_1 and β_2 are two coefficients weighting respectively the non-overlapping constraint and the competition term with respect to the data term

In order to roughly extract the class of interest from point cloud, a scatter descriptor [20] is used to identify the points which potentially correspond to trees.

D Performance tests on conventional Markov Random Field models

As mentioned in the paper, our Monte Carlo sampler can be used for optimizing conventional multi-label energies of the form:

$$U(l) = \sum_{i \in \mathcal{V}} D_i(l_i) + \sum_{(i,j) \in \mathcal{E}} V(l_i, l_j) \tag{27}$$

where $\mathcal{V}$ is the set of vertices (or sites in case of images), $\mathcal{E}$ is the set of edges (i.e. pairs of neighboring vertices), and $l \in [1, N]^{card(\mathcal{V})}$ is a configuration of labels over $\mathcal{V}$ with N, the number of

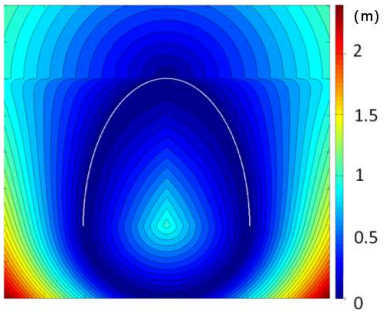

Figure 17: behavior of d in the XZ-plane - The isocurves represent the distances from points to the semi-ellipsoidal surface colored in white.

labels of the problem. More details concerning this type of energy minimization problems can be found in [21].

Indeed, the point processes can be seen as a generalization of these conventional MRF models, where
(i) the dimension of the configuration space is variable (graph structure is not static but dynamic),
(ii) labels are defined in discrete or/and continuous domains so that complex parametric objects can be handled,
(iii) there is no constraint on the form of the pairwise interaction term V by the minimization techniques.

A uniform distribution of the labels is considered here. Indeed there is no point to compute a partitioning tree from a predefined segmentation as the problem is to segment the data. A regular partitioning is then used, as illustrated on Figure 2- (c) and (d) of the paper. The width of a cell is given by the cell independence condition (see Eq. 8 in the paper). As $\delta_{max} = 0$ (objects are fixed), the width of cells must be superior or equal to ϵ,*i.e.* the width of the neighborhood relationship. For instance in case of an image labeling problem with a 4- or 8-connexity neighborhood, the condition implies that each cell can contain one unique pixel. Such partitioning is obviously promising as one quarter of all the pixels of the image will be perturbed simultaneously at each iteration of the sampling.

The performances of our sampler have been tested from a basic model of image segmentation. The unitary data term $D_i(l_i)$ measures the quality of label l_i at pixel i via Gaussian distributions. More precisely, the radiometry distribution of each class is modeled by a Gaussian law whose mean and standard deviation are model parameters to be estimated or fixed by an user. The potential V corresponds to the conventional Potts model [22] so that the labeling is smoothed in a local neighborhood (*i.e.* 4-connexity).

Table 3 and Figure 18 show the performances obtained from various images and provide comparisons with the standard optimization techniques, *i.e.* max-product Belief Propagation (BP) [23], Graph-Cut based algorithms [24] and Iterated Conditional Modes (ICM) [25]. Our sampler competes well with the other algorithms. The reached energy is usually slightly higher than by using α-expansion, α-β swap or BP, but the computation time are lower. The gain of time

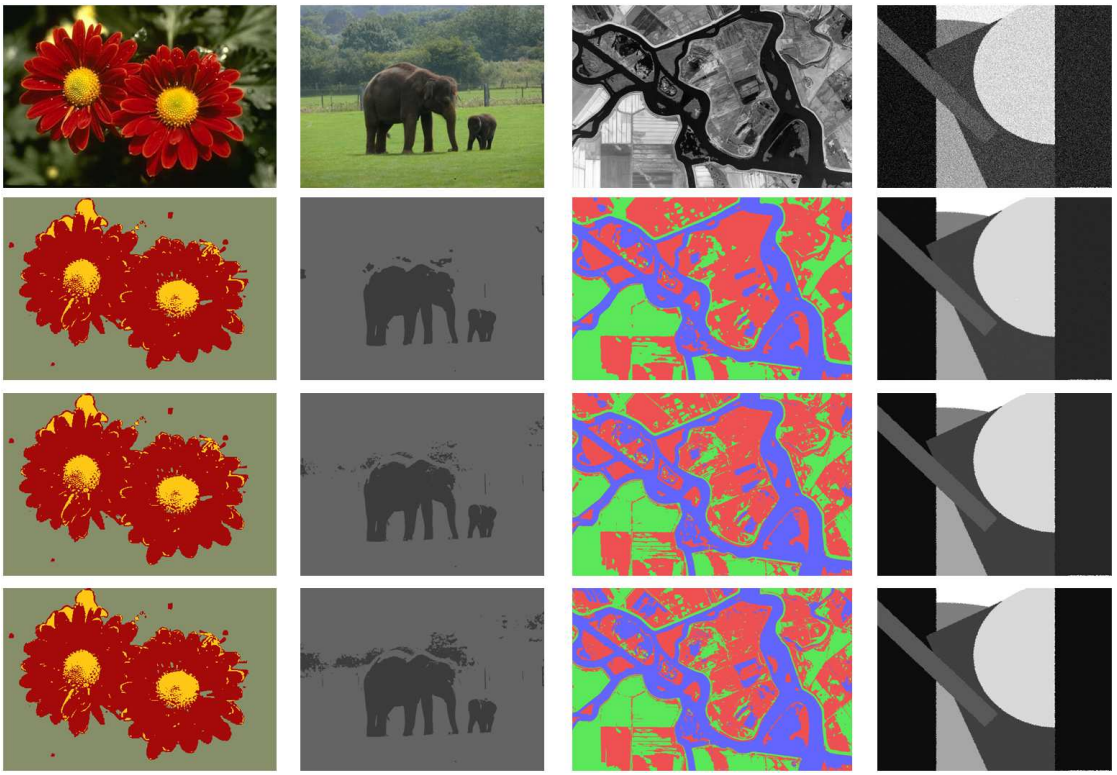

Figure 18: Image segmentation. (top) Input images (from left to right: Flowers, Elephant, Aerial and Simulated). (second row) Results obtained by our sampler, by (third row) α-expansion, and by (last row) ICM. The goal here is not to evaluate the segmentation model which is obviously not optimal, but to compare the results from various optimization techniques, in particular from α-expansion and ICM which provide the lowest and highest energies in the mean respectively.

	our sampler		α-expansion		α-β swap		BP		ICM	
	energy	time	energy	time	energy	time	energy	time	energy	time
Flowers 3 labels 154k pixels	1.4455	**0.48**	**1.4453**	1.47	1.4453	1.59	1.4453	3.92	1.4460	1.17
Elephant 2 labels 9.98M pixels	40.74	**40.01**	40.64	45.22	40.64	73.84	**40.63**	209.7	40.77	55.5
Aerial 3 labels 943k pixels	2.7210	**3.3**	**2.7190**	7.77	2.7192	10.8	2.7210	18.49	2.8303	7.94
Simulated 8 labels 260k pixels	1.3192	**0.92**	1.3187	6.759	1.3186	7.71	**1.3185**	8.25	4.1186	4.7

Table 3: Performances of various optimization algorithms in terms of reached energy and computation time (expressed in second) from the images shown in Fig. 18.

becomes very attractive when the number of labels and the image size increase. In particular, the results obtained from *Simulated*, which is a simulated image of 8 classes which has been corrupted by a Gaussian noise, show that our sampler can be an interesting alternative to the standard optimization techniques by strongly reducing computation times while reaching an energy of similar quality. Note that the energy value from the ICM algorithm is very bad on this image (4.1186). Indeed ICM gets stuck in local minima as illustrated in Fig. 18-(bottom right image) where the entire right cluster has been incorrectly classified (back color instead of dark grey).
These preliminary experiments presented in this appendix are promising, but need to be developed. In particular, comparisons with parallelizable versions of graph-cut based algorithms, e.g. [26], must be led to evaluate more deeply the potential of the sampler for solving multi-label MRF problems.

E Additional results and comparisons

We present in this appendix some additional results and comparisons on population counting and line-network extraction problems. Note that the following images have been captured in high resolution. The reader is invited to zoom in the images in order to see more details.

- Fig. 19, 20 and Tab. 4 propose results on cell counting from microscope images. These images have been simulated by [27] and are provided with ground truth, i.e. the exact number and location of cells are known for each image. Our algorithm has been compared to the supervised approach proposed by Lempitsky et al. [19] in Tab. 4. Note that, contrary to our algorithm, this supervised approach just delivers an estimated number of cells per images without locating and delineating them.

- Fig. 21 and Tab. 5 present additional line-network results. Fig. 21 shows visual comparisons with different approaches [18, 28, 7] from both the road image presented in Fig. 6 of the paper and an aerial image of a river-network. Similarly to Tab. 1 of the paper, Tab. 5 provides a comparison with [18, 28, 7] from the river image in terms of computation time and network extraction accuracy.

- Fig. 22, 23 and 24 show results on different object extraction problems from images.

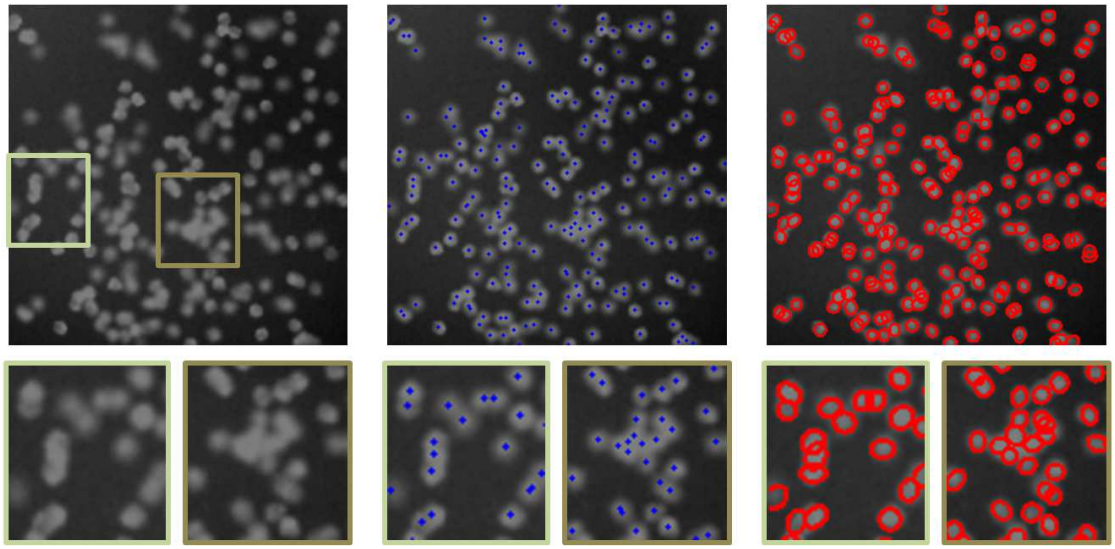

Figure 19: Cell counting from (left) the microscope image *cell17*. (middle) Ground Truth shows the location of each cell through a blue cross. (right) Our 2D point process of ellipses captures the cells with very few errors. As illustrated on the right crop, omissions can appear when many cells are regrouped in a tiny area. Note that, in such a case, it is very difficult to visually detect the cells, even for an expert.

	cell17	*cell18*	*cell19*	*cell20*	*cell21*	*cell22*	*cell23*
Ground Truth	213	185	188	169	149	184	161
Our algorithm	209	184	187	169	147	184	159
Lempitsky et al. [19] ($L1$-regularisation)	202.9	184.6	192.2	174.1	148.6	182.6	158.3
Lempitsky et al. [19] (Tikhonov-regularisation)	194.1	175.9	180.1	170.4	144.4	176.5	157.6

Table 4: Comparisons with the cell counting approach proposed by Lempitsky et al. [19] from the microscope images of Fig. 19 and 20. The values correspond to the number of cells in the considered image. Our algorithm provides a better estimation of the number of cells than both the $L1$- and Tikhonov-regularization versions of [19]. In particular, our algorithm is more accurate in case of configurations of cells highly concentrated in small areas.

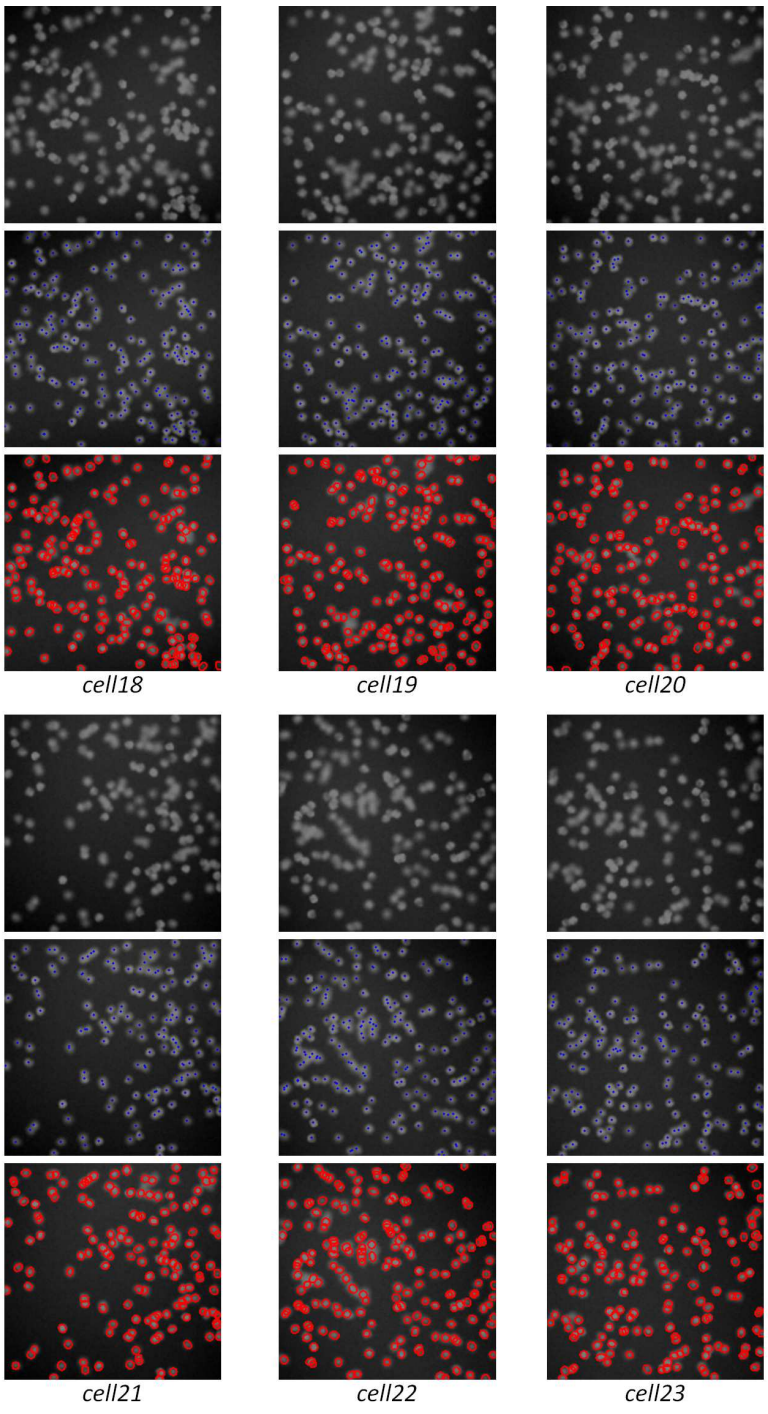

Figure 20: Cell counting from a set of six microscope images. Similarly to Fig. 19, Ground Truth is represented by (middle) the blue crosses whereas our result is given by (bottom) the red ellipses.

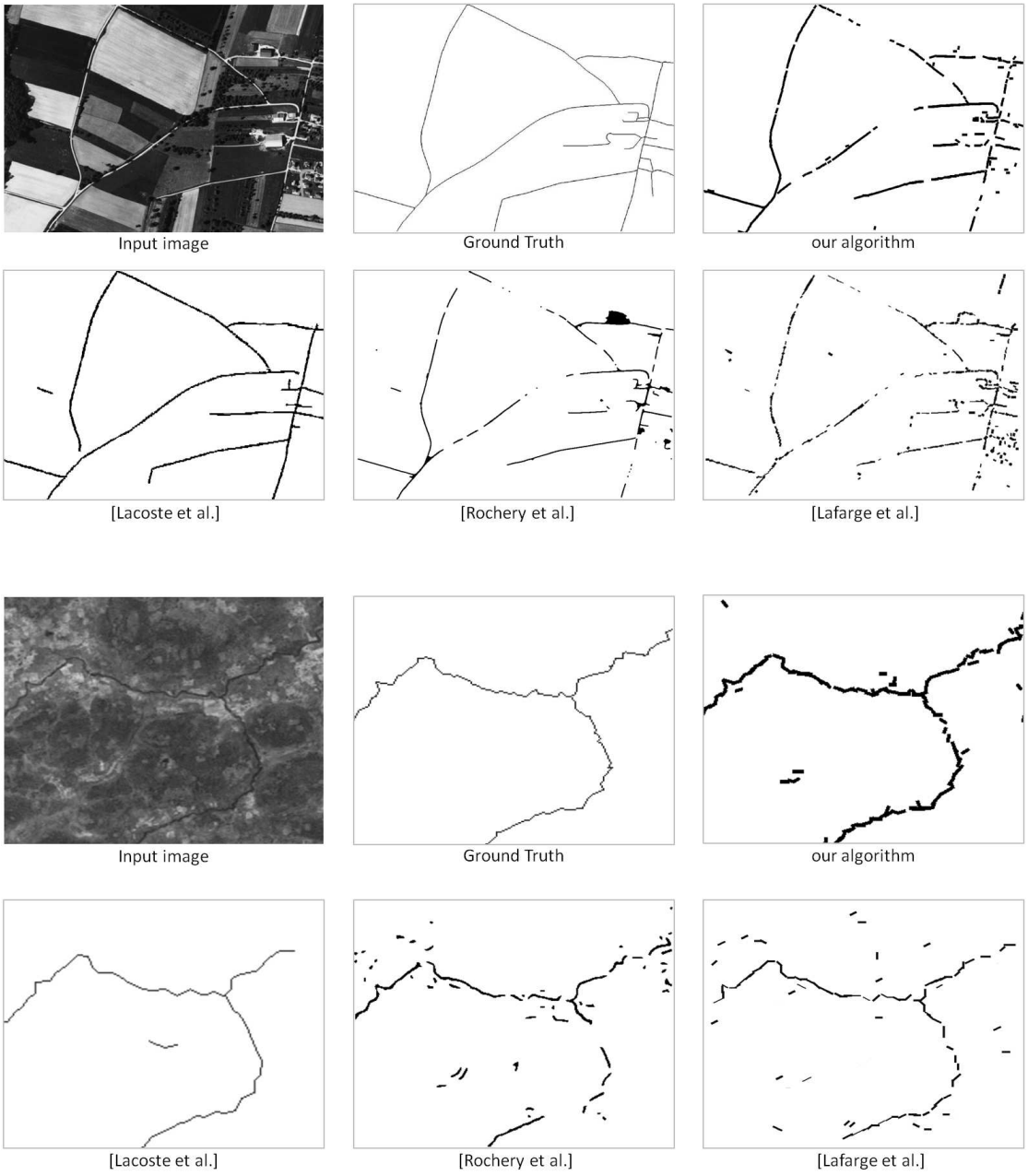

Figure 21: Line-network extraction. Our algorithm gives more accurate results than the methods proposed by Rochery et al.[18] and Lafarge et al.[28] from (top) the road- and (bottom) river-network images, but does not perform better than Lacoste et al.[7] which propose a more complex model with many geometric interactions to structure the line-segments together (also implying many model parameters to be tuned). As detailed in Tab. 1 of the paper and Tab. 5, our sampler significantly reduces the computation time compared to these three methods.

	our sampler	Lafarge et al.[28]	Lacoste et al.[7]	Rochery et al.[18]
Time (minute)	0.28	1.8	45	10
Over-detection	0.78%	1.36%	0.22%	1.68%
Under-detection	30.5%	35.4%	32%	39.8%
Representation	line-segment	line-segment	line-segment	pixels

Table 5: Comparison with existing line-network extraction methods from the river image presented in Fig. 21-bottom. Similarly to the comparison from the road image, the result quality in terms of road under/over-detection is higher than [28] and [18], but lower than [7]. Our sampler is clearly faster than the other approaches. Note however that the gain of time is not so important than for the road image which is a much bigger image.

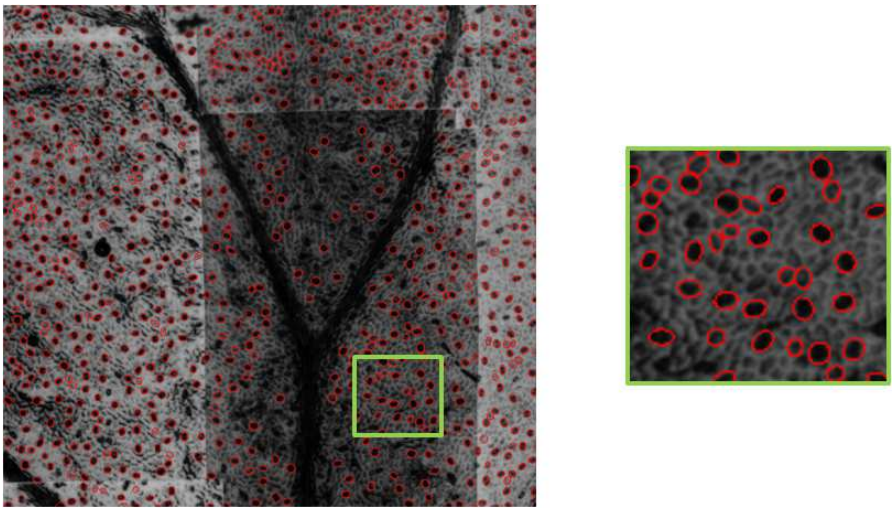

Figure 22: Stomate counting. Counting and extracting opened stomata on leaf permits us to analyze the adverse environmental condition. Indeed, the plant reacts to stressful phenomena such as air pollution by closing stomata. Our 2D point process captures opened stomata (black marks) by ellipses from mosaic images. 757 stomata are detected in 168 seconds from the left image. Note at right how opened stomata are correctly extracted in spite of the high density of the close stomata (low contrasted marks).

Figure 23: Taxi detection. The urban traffic of taxis is analyzed by counting and extracting yellow cabs from aerial images. Our 2D point process captures taxis by ellipses. Note that the Bhattacharya distance has been adapted to favor the yellow objects in the image. 87 taxis are detected in 165 seconds from the left image. As shown on the left, our algorithm allows the localization of taxis in spite of the presence of other vehicles.

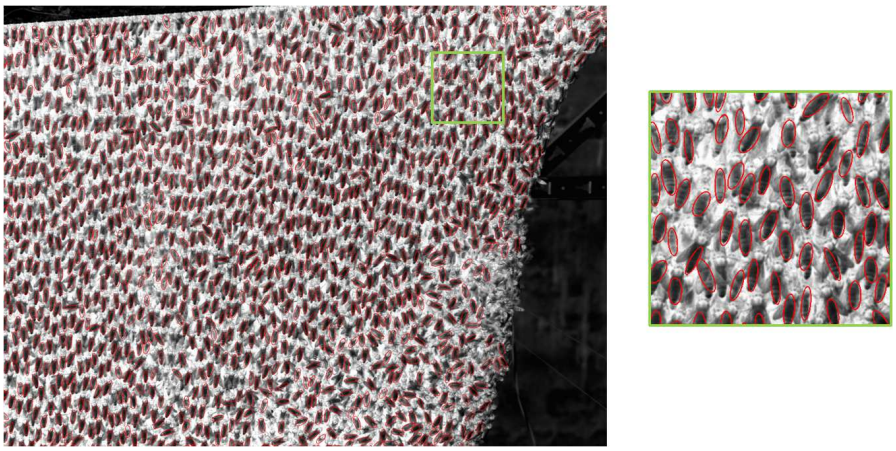

Figure 24: Bee extraction. Counting and tracking bees in beehives allows us to analyze the behavior of bees from a general point of view. Our 2D point process captures bee bodies by ellipses from images of beehives. 1167 bees are detected in 12 minutes from the left image. As shown on the cropped image, the bees are globally well detected in spite of the high density and bee overlap. Note that the computing time is high compared to other applications because the partitioning scheme contains few cells, *i.e.* 75.

References

[1] Baddeley, A.J., Lieshout, M.V.: Stochastic geometry models in high-level vision. Journal of Applied Statistics **20** (1993)

[2] Descombes, X., Minlos, R., Zhizhina, E.: Object extraction using a stochastic birth-and-death dynamics in continuum. Journal of Mathematical Imaging and Vision **33** (2009)

[3] Ge, W., Collins, R.: Marked point processes for crowd counting. In: CVPR, Miami, U.S. (2009)

[4] Lafarge, F., Gimel'farb, G., Descombes, X.: Geometric feature extraction by a multi-marked point process. PAMI **32** (2010)

[5] Lieshout, M.V.: Depth map calculation for a variable number of moving objects using markov sequential object processes. PAMI **30** (2008)

[6] Mallet, C., Lafarge, F., Roux, M., Soergel, U., Bretar, F., Heipke, C.: A marked point process for modeling lidar waveforms. IP **19** (2010)

[7] Lacoste, C., Descombe, X., Zerubia, J.: Point processes for unsupervised line network extraction in remote sensing. PAMI **27** (2005)

[8] Sun, K., Sang, N., Zhang, T.: Marked point process for vasculartree extraction on angiogram. In: EMMCVPR, Ezhou, China (2007)

[9] Utasi, A., Benedek, C.: A 3-D marked point process model for multi-view people detection. In: CVPR, Colorado Springs, U.S. (2011)

[10] Green, P.: Reversible Jump Markov Chains Monte Carlo computation and Bayesian model determination. Biometrika **82** (1995)

[11] Hastings, W.: Monte Carlo sampling using Markov chains and their applications. Biometrika **57** (1970)

[12] Han, F., Tu, Z.W., Zhu, S.: Range image segmentation by an effective jump-diffusion method. PAMI **26** (2004)

[13] Srivastava, A., Grenander, U., Jensen, G., Miller, M.: Jump-Diffusion Markov processes on orthogonal groups for object pose estimation. Journal of Statistical Planning and Inference **103** (2002)

[14] Tu, Z., Zhu, S.: Image Segmentation by Data-Driven Markov Chain Monte Carlo. PAMI **24** (2002)

[15] Harkness, M., Green, P.: Parallel chains, delayed rejection and reversible jump mcmc for object recognition. In: BMVC, Bristol, U.K. (2000)

[16] Byrd, J., Jarvis, S., Bhalerao, A.: On the parallelisation of mcmc-based image processing. In: IEEE International Symposium on Parallel and Distributed Processing, Atlanta, U.S. (2010)

[17] Gonzalez, J., Low, Y., Gretton, A., Guestrin, C.: Parallel Gibbs sampling: From colored fields to thin junction trees. Journal of Machine Learning Research (2011)

[18] Rochery, M., Jermyn, I., Zerubia, J.: Higher order active contours. IJCV **69** (2006)

[19] Lempitsky, V., Zisserman, A.: Learning to count objects in images. In: NIPS, Vancouver, Canada (2010)

[20] Toshev, A., Mordohai, P., Taskar, B.: Detecting and parsing architecture at city scale from range data. In: CVPR, San Francisco, US (2010)

[21] Szeliski, R., Zabih, R., Scharstein, D., Veksler, O., Kolmogorov, V., Agarwala, A., Tappen, M., Rother, C.: Comparative study of energy minimization methods for markov random fields with smoothness-based priors. PAMI **30** (2008)

[22] Li, S.: Markov Random Field Modeling in Image Analysis. Springer (2001)

[23] Weiss, Y., Freeman, W.: On the optimality of solutions of the max-product belief propagation algorithm in arbitrary graphs. IEEE Trans. on Information Theory **47** (2001)

[24] Boykov, Y., Veksler, O., Zabih, R.: Fast approximate energy minimization via graph cuts. PAMI **23** (2001)

[25] Besag, J.E.: On the statistical analysis of dirty pictures. Journal of the Royal Statistical Society **48** (1986)

[26] Vineet, V., Narayanan, P.: Solving multi-label MRFs using incremental alpha-expansion move on the GPUs. In: ACCV, Xi'an, China (2009)

[27] Lehmussola, A., Ruusuvuori, P., Selinummi, J., Huttunen, H., Yli-Harja, O.: Computational framework for simulating fluorescence microscope images with cell populations. IEEE Trans. on Medical Imaging **26** (2007)

[28] Lafarge, F., Gimel'farb, G.: Texture representation by geometric objects using a jump-diffusion process. In: BMVC, Leeds, U.K. (2008)

Contents

1 Introduction **3**
1.1 Point processes for vision problems 3
1.2 Motivations 3
1.3 Contributions 4

2 Point Process background **5**

3 New sampling procedure **6**
3.1 Simultaneous multiple perturbations 6
3.2 Non-uniform point distributions 9
3.3 Sampler formulation 11

4 Experiments **12**
4.1 Implementation 12
4.2 Point processes in 2D 12
4.3 Point processes in 3D 14

5 Conclusion **16**

Appendices **17**

A Details on the population counting model from images **17**

B Details on the line-network extraction model from images **18**

C Details on the tree recognition model from 3D point clouds **20**

D Performance tests on conventional Markov Random Field models **22**

E Additional results and comparisons **25**

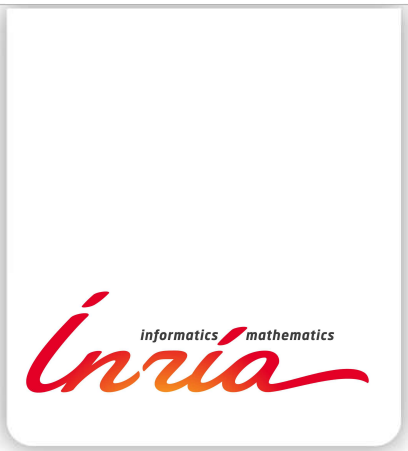

RESEARCH CENTRE
SOPHIA ANTIPOLIS – MÉDITERRANÉE

2004 route des Lucioles - BP 93
06902 Sophia Antipolis Cedex

Publisher
Inria
Domaine de Voluceau - Rocquencourt
BP 105 - 78153 Le Chesnay Cedex
inria.fr

ISSN 0249-6399